Astronomy & Astrophysics

The HELLAS2XMM survey

XIII. Multi-component analysis of the spectral energy distribution of obscured AGN

F. Pozzi[1,2], C. Vignali[1,2], A. Comastri[2], E. Bellocchi[3], J. Fritz[4], C. Gruppioni[2], M. Mignoli[2], R. Maiolino[5], L. Pozzetti[2], M. Brusa[6], F. Fiore[5], and G. Zamorani[2]

[1] Dipartimento di Astronomia, Università degli Studi di Bologna, via Ranzani 1, 40127 Bologna, Italy
  e-mail: f.pozzi@unibo.it
[2] INAF - Osservatorio Astronomico di Bologna, via Ranzani 1, 40127 Bologna, Italy
[3] Instituto de Estructura de la Materia (IEM/CSIC), C/ Serrano 121, 28006 Madrid, Spain
[4] Sterrenkundig Observatorium, Vakgroep Fysica en Sterrenkunde, Universeit Gent, Krijgslaan 281, S9 9000 Gent, Belgium
[5] INAF - Osservatorio Astronomico di Roma, via di Frascati 33, 00040 Roma, Italy
[6] Max Planck Institut für Extraterrestrische Physik (MPE), Giessenbachstrasse 1, 85748 Garching bei München, Germany

ABSTRACT

Aims. We combine near-to-mid-IR *Spitzer* data with shorter wavelength observations (optical to X-rays) to get insight into the properties of a sample of luminous, obscured active galactic nuclei (AGN). We aim at modelling their broad-band spectral energy distributions (SEDs) in order to estimate the main parameters related to the dusty torus that is assumed to be responsible for the reprocessed IR emission. Our final goal is to estimate the intrinsic nuclear luminosities and the Eddington ratios for our luminous, obscured AGN.
Methods. The sample comprises 16 obscured high-redshift ($0.9 \lesssim z \lesssim 2.1$), X-ray luminous quasars ($L_{2-10\ \mathrm{keV}} \sim 10^{44}$ erg s^{-1}) selected from the HELLAS2XMM survey in the 2–10 keV band. The optical-IR SEDs are described by a multi-component model that includes a stellar component to account for the optical and near-IR emission, an AGN component that dominates in the mid-IR (mainly emission from a dusty torus heated by nuclear radiation), and a starburst to reproduce the far-IR bump. A radiative transfer code to compute the spectrum and intensity of dust reprocessed emission was extensively tested against our multiwavelength data. While the torus parameters and the BH accretion luminosities are a direct output of the SED-fitting procedure, the BH masses were estimated indirectly by means of the local $M_{\mathrm{bulge}}-M_{\mathrm{BH}}$ relation.
Results. The majority ($\sim$80%) of the sources show moderate optical depth ($\tau_{9.7\ \mu m} \leq 3$), and the derived column densities N_{H} are consistent with the X-ray inferred values ($10^{22} \lesssim N_{\mathrm{H}} \lesssim 3 \times 10^{23}$ cm^{-2}) for most of the objects, confirming that the sources are moderately obscured Compton-thin AGN. Accretion luminosities in the range $5 \times 10^{44} \lesssim L_{\mathrm{bol}} \lesssim 4 \times 10^{46}$ erg s^{-1} are inferred from the multiwavelength fitting procedure. We compare model luminosities with those obtained by integrating the observed SED, finding that the latter are lower by a factor of $\sim$2 in the median. The discrepancy can be as high as an order of magnitude for models with high optical depth ($\tau_{9.7\ \mu m} = 10$). The ratio between the luminosities obtained by the fitting procedure and from the observed SED suggest that, at least for type 2 AGN, observed bolometric luminosities are likely to underestimate intrinsic ones and the effect is more severe for highly obscured sources. Bolometric corrections from the hard X-ray band are computed and have a median value of $k_{2-10\ \mathrm{keV}} \sim 20$. The obscured AGN in our sample are characterized by relatively low Eddington ratios (median $\lambda_{\mathrm{Edd}} \sim 0.08$). On average, they are consistent with the Eddington ratio increasing at increasing bolometric correction.

Key words. quasars: general – galaxies: nuclei – galaxies: active

1. Introduction

A robust determination of active galactic nuclei (AGN) spectral energy distributions (SEDs) is of paramount importance to better understand the accretion processes onto supermassive black holes (SMBHs) and their cosmological evolution. According to our present knowledge, the bulk of accretion luminosity is emitted in the optical-UV range with a quasi-thermal spectrum originating in an optically thick, geometrically thin, accretion disk. Electrons with temperatures of a few hundreds of keV form a hot corona that upscatters disk photons to X-ray energies with a power-law spectrum and an exponential high-energy cut-off corresponding to the electron temperature (e.g., Haardt & Maraschi 1991). Dusty material, possibly with a toroidal geometry, intercepts a fraction of the primary continuum, which depends on the

covering factor. The absorbed energy is re-emitted in the near-to-far infrared with a grey-body spectral shape.

The SED of optically bright, unobscured QSO is relatively well known. After the seminal work of Elvis et al. (1994), fairly accurate measurements were published by Richards et al. (2006) using Sloan Digital Sky Survey (SDSS) data. The emission is characterized by a double bump. In a νF_ν diagram, the optical-UV spectrum rises steeply towards the shortest accessible wavelengths. It is commonly referred to as the Big Blue Bump and thought to be the accretion disk signature. The IR bump is weaker and likely due to a dusty torus seen almost face-on. The ratio between UV (at 2500 Å) and X-ray luminosity (at 2 keV), parameterized by the slope α_{ox}[1] of the power law connecting the

---

[1] $\alpha_{\mathrm{ox}} = -\frac{\log(f_{2\ \mathrm{keV}}/f_{2500\ \text{Å}})}{\log(\nu_{2\ \mathrm{keV}}/\nu_{2500\ \text{Å}})}$, Zamorani et al. (1981).

rest-frame luminosities, increases with increasing UV luminosity (e.g., Vignali et al. 2003; Steffen et al. 2006).

The average SEDs for radio-loud and radio-quiet type 1 AGN presented in Elvis et al. (1994) allow estimation of bolometric corrections, which are a key parameter in determining the bolometric luminosity from observations at a given frequency, and the Eddington ratio, once the SMBH mass is known. By including the α_{ox} vs. UV luminosity dependence, Marconi et al. (2004) and Hopkins et al. (2006) have computed luminosity-dependent bolometric corrections and adopted them for estimating the local SMBH mass density from the observed X-ray luminosity functions.

The luminosity dependence of bolometric corrections has recently been questioned by Vasudevan & Fabian (2009), who point out the importance of simultaneous optical-UV and X-ray observations and reddening corrections in the UV. They suggest that the bolometric correction correlates with the Eddington ratio rather than with the bolometric luminosity. Their observational results align with the predictions of accretion disk models (e.g., Witt et al. 1997) where higher blue-bump to X-ray ratios for sources with higher Eddington ratios are expected.

While significant progress has been made towards a better determination of type 1 AGN SEDs, our knowledge of type 2 broad-band spectra is much more limited even though most of the accretion-driven energy density in the Universe is expected to occur in obscured AGN (e.g., Fabian 1999; Gilli et al. 2007, and references therein). Therefore, a robust estimate of their bolometric luminosity is extremely important for properly addressing the issue of SMBH evolution over cosmic time.

Nuclear accretion luminosity in type 2 AGN is very faint in the optical-UV and soft X-rays. Moreover, the host galaxy stellar light often dominates in the optical, making it difficult to disentangle nuclear emission from starlight. Infrared emission is only marginally affected by dust obscuration and has proved to be a powerful indicator of dust-obscured AGN. In particular, the thermally reprocessed nuclear emission of obscured type 2 AGN is expected to peak around a few tens of microns (e.g., Fritz et al. 2006, hereafter F06, and references within).

Mid-IR (MIR) observations, especially those obtained in the past few years with the *Spitzer* satellite, are extremely efficient in studying obscured AGN (e.g. Rigby et al. 2005; Martínez-Sansigre et al. 2005; Weedman et al. 2006; Fiore et al. 2008). In a previous paper (Pozzi et al. 2007), we presented the first analysis of the mid-IR data of a *Spitzer* programme devoted to systematic study of the broad-band properties of X-ray selected, luminous obscured quasars. In Pozzi et al. (2007), the SEDs were reproduced by means of SED templates from Silva et al. (2004).

Here we present the observational data for our final sample of 16 obscured quasars and the detailed modelling of their broad-band SED using a more complete multi-component model, with goodness of fit estimated via χ^2 analysis.

The outline of the paper is as follows. In Sect. 2 the X-ray selected quasar sample is presented, along with all the available multi-band (optical, near-IR (NIR) and sub-mm) and spectroscopic follow-up. The *Spitzer* data are presented in Sect. 3, with data reduction and analysis. In Sect. 4, the complete multi-component model is described. In Sect. 5, the best-fitting solutions are discussed, while in Sect. 6 we focus on the black hole physical properties that can be constrained from the best-fitting procedure. Finally, the main results are summarized in Sect. 7.

Hereafter, we adopt the concordance cosmology ($H_0 = 70$ km s^{-1} Mpc^{-1}, $\Omega_m = 0.3$, and $\Omega_\Lambda = 0.7$, Spergel et al. 2003). Magnitudes are expressed in the Vega system.
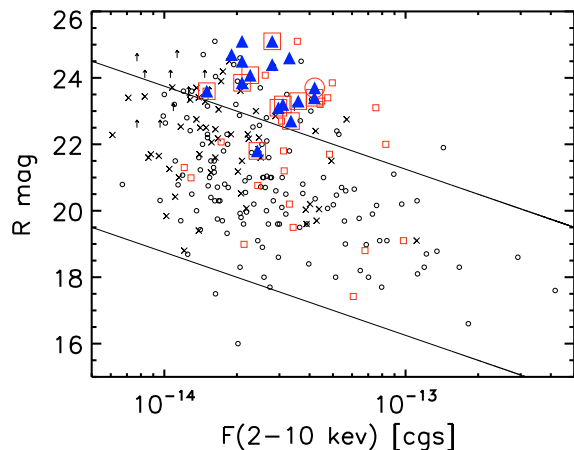
Fig. 1. *R*-band magnitudes vs. hard X-ray (2–10 keV) flux for the full HELLAS2XMM sample (Cocchia et al. 2007). Blue triangles represent the sources included in the present analysis: blue triangles inside red symbols represent the sources with spectroscopic redshifts. Other symbols: empty red squares = sources spectroscopically classified as type 2 AGN; empty circles = sources spectroscopically classified as non-type 2 AGN (type 1 AGN, emission-line galaxies, early-type galaxies and groups/clusters of galaxies); crosses: objects not observed spectroscopically; upward arrows = lower limits. The dashed lines represent the loci of constant X/O ratio (X/O = ±1).

2. The sample

The sample presented in this work comprises 16 X-ray obscured quasars detected in the HELLAS2XMM survey (Baldi et al. 2002) and observed by *Spitzer* in 2006. The HELLAS2XMM survey is a shallow, large-area, hard X-ray survey ($S_{2-10\,keV} > 10^{-14}$ erg cm^{-2} s^{-1}) over a final area of 1.4 deg^2. The catalogue comprises 232 X-ray sources; ~92% of the sample is optically identified down to $R \sim 25$, while ~70% of the sources have a spectroscopic classification (Fiore et al. 2003; Maiolino et al. 2006; Cocchia et al. 2007).

The 16 sources were selected from the original survey to include the most luminous obscured quasars. The selection was primarily based on the X-ray-to-optical flux ratio (hereafter X/O)[2], which has been proven to be an efficient way of selecting high-redshift ($z \gtrsim 1$), obscured quasars (see Fiore et al. 2003). All but one of the sources were selected to have X/O greater than 1 (see Fig. 1 and Table 1), with the only exception GD 158#19 (X/O ~ 0.63), which was included in the sample for its peculiar properties (see Vignali et al. 2009, hereafter V09). We note, however, that not all of the HELLAS2XMM sources matching this selection criterion are present in this work.

The selected sources are relatively faint in the optical band, with an *R*-band magnitude in the range 21.8–25.1 (the brightest object being the peculiar source GD 158#19). By combining optical photometry with deep K_s-band photometry (obtained with the Infrared Spectrometer And Array Camera, *ISAAC*, mounted on the ESO-VLT1 Telescope), almost all the objects are found to be extremely red sources (EROs, $R - K_s \geq 5$). The link between high X/O ratios and optical-to-near colours was studied by e.g., Brusa et al. (2005). Considering different X-ray surveys at different depths, they find a clear trend: the higher X/O, the redder the source.

In Mignoli et al. (2004), detailed K_s-band morphological studies were presented for 8 objects of the sample selected from

---

[2] X/O is defined as $\log \frac{F_X}{F_R}$. We used $f_R(0) = 1.74 \times 10^{-9}$ erg cm^{-2} s^{-1} Å^{-1} and $\Delta\lambda_R = 2200$ Å, Zombeck (1990).

Table 1. Properties of our luminous obscured quasars.

Complete name	Abbreviation	2–10 keV flux^a	R^b	$K_s{}^c$	X/O	z^d	$N_H{}^e$	$L_{2-10\,\mathrm{keV}}{}^f$
HELLAS2XMM 054022.0-283139	PKS 0537#43	3.35	22.70	17.50	1.10	1.797	$10.5^{9.4}_{4.8}$	6.8
HELLAS2XMM 053920.4-283721	PKS 0537#11a	4.19	23.40	18.25	1.48	0.981	$1.3^{1.5}_{0.9}$	1.9
HELLAS2XMM 053917.1-283819	PKS 0537#164	1.50	23.60	19.02	1.12	1.824	–	3.1
HELLAS2XMM 053851.3-283949	PKS 0537#123	2.97	23.10	17.94	1.21	1.153	$6.6^{21.6}_{4.1}$	2.0
HELLAS2XMM 003413.8-115559	GD 158#62	3.59	23.30	21.83	1.38	1.568	$26.3^{44.7}_{18.1}$	4.9
HELLAS2XMM 003357.2-120039	GD 158#19	2.43	21.80	–	0.63	1.957	$7.3^{11.7}_{5.5}$	6.3
HELLAS2XMM 204428.7-105629	Mrk 509#01	2.10	23.85	17.88	1.36	1.049	<1.1	1.5
HELLAS2XMM 204349.7-103243	Mrk 509#13	3.10	23.99	18.79	1.59	1.261	$2.5^{4.6}_{2.2}$	2.6
HELLAS2XMM 235956.6-251019	Abell 2690#75	3.30	24.60	18.33	1.85	$1.3^{+0.30\dagger}_{-0.20}$	$15.0^{20.0}_{8.5}$	3.2
HELLAS2XMM 031343.5-765426	PKS 0312#36	1.90	24.70	19.13	1.66	$0.9^{+0.05\dagger}_{-0.15}$	$1.0^{1.2}_{0.9}$	0.7
HELLAS2XMM 054021.1-285037	PKS 0537#91	4.2	23.70	18.99	1.60	1.538	$45.9^{102.0}_{36.0}$	8.1
HELLAS2XMM 053945.2-284910	PKS 0537#54	2.1	25.10	18.91	1.86	$>1.3^\dagger$	–	2.0
HELLAS2XMM 053911.4-283717	PKS 0537#111	2.1	24.50	17.64	1.62	$1.2^{+0.20\dagger}_{-0.10}$	$9.1^{12.4}_{5.3}$	1.7
HELLAS2XMM 000111.6-251202	Abell 2690#29	2.8	25.10	17.67	1.99	2.08	$2.1^{2.6}_{1.6}$	8.4
HELLAS2XMM 031018.9-765957	PKS 0312#45	2.8	24.40	18.62	1.70	$1.85^{+0.20\dagger}_{-0.30}$	$8.0^{8.4}_{4.6}$	6.2
HELLAS2XMM 005030.7-520046	BPM 16274#69	2.27	24.08	17.87	1.48	1.35	$2.5^{1.5}_{1.0}$	2.4

Notes. $^{(a)}$ Fluxes in units of 10^{-14} erg cm^{-2} s^{-1} from Perola et al. (2004) (with the exception of BPM 16274#69, from Lanzuisi et al., in preparation); $^{(b)}$ magnitude from Fiore et al. (2003) (with the exception of source BPM 16274#69, from Cocchia et al. 2007); $^{(c)}$ for a sub-sample of sources, the K_s-band analysis can be found in Mignoli et al. (2004); $^{(d)}$ spectroscopic redshift from optical spectroscopy (Fiore et al. 2003) and, for three sources, from near-IR spectroscopy (Abell 2690#29 and BPM 16274#69 from Maiolino et al. 2006; PKS 0537#91 from Sarria et al., in preparation); photometric redshifts ($^{(\dagger)}$ symbol), and corresponding 1σ errors, from Pozzi et al. (2007); $^{(e)}$ column densities in source rest-frame in units of 10^{22} cm^{-2} measured from X-ray spectral fitting (see Perola et al. 2004; and Lanzuisi et al., in preparation). For the sources with photometric redshifts, values are taken from Pozzi et al. (2007). For PKS 0537#164 the X-ray spectral fitting is prevented by the few X-ray counts; for Mrk 509#01, only an upper limit was derived (Perola et al. 2004); for PKS 0537#54, the column density is 9.3×10^{22} cm^{-2} for $z = 1.3$. Galactic absorption column densities adopted in the spectral fitting are: 8×10^{20} cm^{-2} for the field PKS 0312$-$77; 2×10^{20} cm^{-2} for the field Abell 2690; 2.1×10^{20} cm^{-2} for the field PKS 0537$-$28; 4×10^{20} cm^{-2} for the field Mrk 509; 2.5×10^{20} cm^{-2} for the field GD 158$-$100 (see Stark et al. 1992); $^{(f)}$ rest-frame, absorption-corrected, X-ray luminosity in units of 10^{44} erg s^{-1} from Perola et al. (2004) and from Pozzi et al. (2007) for sources with photometric redshifts. Luminosities are computed using $H_0 = 70$ km s^{-1} Mpc^{-1}, $\Omega_m = 0.3$ and $\Omega_\Lambda = 0.7$.

those sources with the more extreme $R - K_s$ colours: the majority of the sources (6 over 8) have an extended K_s-band morphology, consistent with an elliptical-type profile, without any evidence of a nuclear point-like source (which would be expected to trace the X-ray AGN). This suggests that the nuclear emission is diluted and hidden by the host galaxy up to at least 2.2 μm. The R and K_s-band magnitudes are reported in Table 1.

Spectroscopic information for 11 sources is available thanks to optical (8 sources, see Fiore et al. 2003; and Cocchia et al. 2007) and near-IR spectroscopy (3 sources, see Maiolino et al. 2006; and Sarria et al., in preparation). All spectra but one are typical of optically obscured AGN, thus confirming the X-ray classification (i.e., type 2). The only exception is source PKS 0537#91, with emission line ratios typical of an HII region (Sarria et al., in preparation). One source, Abell 2690#29, shows the typical rest-frame spectrum of a high-redshift, dust-reddened quasar, with a broad Hα line and a type 1.9 classification (Maiolino et al. 2006). Spectroscopic redshift z are in the range 0.9–2.08 and are reported in Table 1. For the sources without redshift (5 out of 16), a photometric redshift was estimated in Pozzi et al. (2007), where the *Spitzer* data reduction and a preliminary SED analysis were presented.

Finally, sub-mm observations were performed for four sources in 2004 October–November. Only one object, GD 158#19 ($z = 1.957$), was detected, while for the others upper limits were gained. Because of its broad-band coverage (up to 850 μm) with good-quality photometric data, the source GD 158#19 was studied in a dedicated work (see V09).

In Table 1 we report source name, 2–10 keV flux, R, and K_s photometry, X/O ratio, the redshift z, the column densities

N_H, and the absorption-corrected (2–10 keV) X-ray luminosities of the sample. The source table order reflects the *Spitzer* observation strategy (see Sect. 3). The sub-mm flux densities are reported in Table 2 along with the fluxes obtained in the IR bands (from 3.6 μm up to 160 μm) with the *Spitzer* satellite (see Sect. 3). Almost all the sources have column densities N_H in the range $10^{22.0}$–$10^{23.4}$ cm^{-2} and 2–10 keV rest-frame luminosities in the range $10^{43.8}$–$10^{44.7}$ erg s^{-1}, placing them in the type 2 quasar population.

3. The *Spitzer* data

The targets were observed by *Spitzer* in 2006 with both IRAC and MIPS instruments in photometry mode. All the sources were observed with the same total integration time in the IRAC bands (480 s), while different strategies were followed in the MIPS bands taking the different optical-NIR properties into account. While all the objects were observed at 24 μm for a total integration time of 1400 s, only a subsample of sources with relatively bright R-band magnitudes ($R < 24$) and spectroscopic redshifts were observed at longer wavelengths, with integration times of 300 s and 600 s at 70 and 160 μm, respectively. PKS 0537#91 (see Table 1) was not observed at 70 and 160 μm since it had no redshift at the epoch of the *Spitzer* observations.

The reduction method is described in detail in Pozzi et al. (2007) and in V09 and it is briefly summarized here. The IRAC flux densities of the sources were measured from the post-basic calibrated data (post-BCD) images in the *Spitzer* archive. Aperture fluxes were measured on the background-subtracted

Table 2. *Spitzer* and *SCUBA* flux densities.

Source name	3.6 μm [μJy]	4.5 μm [μJy]	5.8 μm [μJy]	8.0 μm [μJy]	24 μm [μJy]	70 μm [mJy]	160 μm [mJy]	450 μm [mJy]	850 μm [mJy]
PKS 0537#43	423 ± 42	918 ± 92	1750 ± 175	3202 ± 320	6879 ± 688	27.0 ± 4.5	39.6 ± 7.8		
PKS 0537#11a	57 ± 6	69 ± 7	95 ± 10	168 ± 17	517 ± 57	<3.6	<24		
PKS 0537#164	21 ± 2	18 ± 2	19 ± 4	23 ± 5	<60	<3.6	<24		
PKS 0537#123	84 ± 9	96 ± 10	113 ± 13	165 ± 17	747 ± 81	< 3.6	<24		
GD 158#62	60 ± 6	91 ± 9	155 ± 17	339 ± 35	1608 ± 164	< 3.6	<24	<74	<6.1
GD 158#19	226 ± 23	387 ± 39	756 ± 76	1547 ± 155	5326 ± 534	27.0 ± 4.5	37.7 ± 7.8	<94.3	8.6 ± 2.1
Mrk 509#01	63 ± 7	51 ± 6	60 ± 11	59 ± 10	<60	<3.6	<24	<82	<6.6
Mrk 509#13	51 ± 6	69 ± 7	110 ± 11	215 ± 17	866 ± 94	<3.6	<24	<75	<6.2
Abell 2690#75	51 ± 5	56 ± 6	89 ± 11	139 ± 15	565 ± 62				
PKS 0312#36	41 ± 4	44 ± 5	40 ± 8	710 ± 9	236 ± 30				
PKS 0537#91	28 ± 4	35 ± 4	42 ± 8	800 ± 10	301 ± 40				
PKS 0537#54	31 ± 4	35 ± 4	50 ± 10	470 ± 8	279 ± 45				
PKS 0537#111	88 ± 9	75 ± 8	41 ± 6	460 ± 7	148 ± 28				
Abell 2690#29	141 ± 14	185 ± 19	260 ± 27	371 ± 38	1012 ± 106				
PKS 0312#45	50 ± 6	62 ± 7	69 ± 10	780 ± 10	249 ± 35				
BPM 16274#69	86 ± 9	92 ± 9	97 ± 11	120 ± 13	286 ± 34				

Notes. The upper limits are given at the 3σ confidence level.

maps within a 2.45″ aperture radius using aperture corrections of 1.21, 1.23,1.38, and 1.58 for the four IRAC bands (following the IRAC Data Handbook). For the MIPS bands, we started the analysis from the basic calibrated data (BCD) at 24 μm and from the median high-pass filtered BCD (fBCD) at 70 and 160 μm, as suggested for faint sources. At 24 μm, the BCD were corrected for a residual flat-fielding dependent on the scan mirror position (see Fadda et al. 2006; Pozzi et al. 2007). We then constructed our own mosaics using the SSC MOPEX software (Makovoz & Marleau 2005). Aperture fluxes were measured within a 7″ aperture radius for the 24 μm band and 16″ aperture radius for the 70 and 160 μm bands. The aperture corrections used were 1.61, 2.07, and 4.1 (see the MIPS Data Handbook). A small aperture radius was used at longer wavelengths (at 160 μm the adopted radius is comparable to half of the PSF *FWHM*) to exclude the contamination by nearby far-infrared sources (see V09). At 24 μm, thanks to a better PSF sampling, two sources (PKS 0312#36 and Abell 2690#29) were deblended using a PSF deconvolution analysis.

All 16 sources were clearly detected in the IRAC bands. At 24 μm, 14 sources (out of 16) were detected above the 5σ level and span almost two orders of magnitude in flux, from ~7000 μJy down to the faintest source, close to the 5σ detection level (~100 μJy). For the two sources without detection, an upper limit (3σ) was estimated from the average noise of the map, derived by making multiple aperture measurements at random locations throughout the residual mosaic after source extraction. The typical average noise (1σ) is 20 μJy. At 70 and 160 μm, as said before, only the brightest R-band sources were observed; among them, only the two most luminous (in the optical band) were detected, PKS 0537#43 and GD 158#19, where the latter is the source described in V09. For the 6 remaining sources, an upper limit (3σ) was estimated from the residual mosaic (see also Frayer et al. 2006) after source extraction, as done at 24 μm. The typical average noise (1σ) is 1.2 mJy at 70 and 8 mJy at 160 μm (consistent with the results obtained in the COSMOS field from Frayer et al. 2009, taking the different integration times into account).

Table 2 reports the target flux densities provided by *Spitzer*. To compute uncertainties, the noise map was added in

quadrature to the systematic uncertainties, assumed to be 10 per cent in the IRAC and MIPS 24 μm bands and 15 per cent at 70 and 160 μm (see IRAC and MIPS Data Handbook).

4. Modelling the spectral energy distribution

The observed optical-to-MIR (or FIR/sub-mm) SEDs can be modelled as the sum of three distinct components: a stellar component, which emits most of its power in the optical/NIR; an AGN component, whose emission peaks in the MIR for obscured quasars and is caused by hot dust heated by UV/optical radiation from gas accreting onto the central SMBH; and a starburst component, which represents the major contribution to the FIR spectrum. In this work, we considered all the three components (see Sects. 4.1, 4.2; and Hatziminaoglou et al. 2008). Since the focus of the paper is on the AGN contribution to the SED, we discuss the hot dust modelling and its uncertainties in more detail.

The hot dust emission in AGN is reproduced using the F06 model. This model follows the formalism developed by different authors (e.g., Pier & Krolik 1992; Granato & Danese 1994; Efstathiou & Rowan-Robinson 1995), where the IR emission in AGN originates in dusty gas around the SMBH with a smooth distribution. The dust grains are heated by high-energy photons coming from the accretion disk, and their thermal and scattering re-emission, mostly at IR wavelengths, is computed by means of the radiative transfer equations. For the dust distribution geometry, different possibilities (i.e. "classical" torus shape, tapered or flared disk) are explored in the literature.

More recently, models considering a clumpy distribution for the dust have been developed (e.g., Nenkova et al. 2002; Hönig et al. 2006; Nenkova et al. 2008). These models successfully explain many recent observations in the mid-IR, such as the strength of absorption and emission features at 9.7 μm and the X-ray variability (Risaliti et al. 2002).

Another possibility for the torus models described above are the disk-wind models (see Elitzur & Shlosman 2006, and references therein), involving a completely different approach. The dusty clouds, responsible for the obscuration, are part of a hydromagnetic wind coming from the accretion disk. On the one hand,

these models are potentially capable of explaining disparate phenomena in AGN (from broad emission to absorption lines and obscuration), providing a hydro-dynamical justification for the persistence of the clouds around the SMBH. On the other hand, a parameterization that takes the observational constraints on the clumpy obscuration into account, thereby supplying a grid of synthetic IR SEDs, does not exist yet (see Elitzur 2008).

A detailed comparison between smooth and clumpy dust distribution models is discussed by Dullemond & van Bemmel (2005) who conclude that both models yield similar SEDs (see also Elitzur 2008; and Nenkova et al. 2008). The main difference is in the strength of the silicate feature observed in absorption in objects seen edge-on, which is, on average, weaker for clumpy models with the same global torus parameters. In clumpy models, in fact, clouds at different distances from the central source can be intercepted by the line of sight, including the innermost clouds, where the silicate feature is in emission given the higher temperature of the dust grains. A systematic comparison of the two model predictions is beyond the scope of the present paper and should be performed on high-quality IR data (i.e. a *Spitzer IRS* spectroscopic sample).

Notwithstanding these limitations, with the present work we aim at extracting the maximum information using the available photometric data. The F06 model adopted in this work is one of the models most tested against both broad-band photometry (F06; Berta et al. 2004; Rodighiero et al. 2007; Hatziminaoglou et al. 2008, 2009; Agol et al. 2009; V09) and Spitzer mid-infrared spectra (F06). Moreover, the F06 model was the first one able to reproduce the quasar mid-IR spectra, considered a very strong constraint to characterize the dust properties in AGN and probe the unified model.

4.1. The AGN-torus component

The F06 code assumes a smooth dust distribution around the central source consisting of a Galactic mixture of silicate and graphite grains. The presence of silicate dust grains is clear from the absorption feature at 9.7 μm seen in most type 2 AGN. The graphite grains are, instead, responsible for the rapid decline in the emission at wavelengths shortwards of a few microns, corresponding to a blackbody emission of about 1500 K, the sublimation temperature of these grains (see F06).

The assumed dust geometry is a flared disk (see Efstathiou & Rowan-Robinson 1995), which is a sphere with the polar cones removed. The internal radius of the dust distribution is defined by the sublimation temperature of the dust itself. To simulate a more realistic shape for the dust distribution, F06 assumes that the dust density can vary both with the radial and the angular coordinates:

$$\rho(r,\theta) = \rho_0 \cdot r^\alpha \cdot e^{-\gamma|\cos(\pi/2-\theta)|} \quad (1)$$

where θ is the angle with respect to the equatorial plane.

The dusty torus is heated by the emission of the inner accretion disk, which represents the input energy to the radiative transfer code. The assumed spectrum for the accretion disk is defined in the 10^{-3} to 20 μm regime (from soft X-rays, i.e. 1.25 keV, to mid-IR) and is parameterized by broken power laws in F06. The specific indices of the power laws are adapted from the Granato & Danese (1994) and the Nenkova (2002) models and are consistent with the broad-band SEDs of a sample of type 1 AGN from the SDSS survey (Hatziminaoglou et al. 2008, see their Figs. 8 and 9).

Along with the thermally re-processed light, the F06 provides, as a function of the line-of-sight and optical depth, the

fraction of the inner accretion disk light not intercepted by the torus and the scattered light. In the following, with the AGN component we will refer to the sum of all the three contributions.

4.2. The stellar and starburst components

The stellar component is modelled as the sum of simple stellar populations (SSP) models of different ages, all assumed to have a common (solar) metallicity. A Salpeter (1955) initial mass function (IMF) with mass in the range (0.15–120 $M_\odot$) is assumed. The SSP spectra have been weighted by a Schmidt-like law of star formation (see Berta et al. 2004):

$$SFR(t) = \frac{T_G - t}{T_G} \times \exp\left(-\frac{T_G - 1}{T_G \tau_{sf}}\right) \quad (2)$$

where T_G is the age of the galaxy (i.e. of the oldest SSP) and τ_{sf} the duration of the burst in units of the oldest SSP (see V09). As in Hatziminaoglou et al. (2008) and V09, a common value of extinction is applied to stars at all ages, by adopting the extinction law of our Galaxy ($R_V = 3.1$; Cardelli et al. 1989).

To keep the number of free parameters as low as possible, emission from cold dust, which dominates the bolometric emission at wavelengths longer than 30 μm rest-frame, is only included when far-IR/sub-mm data allow us to constrain that part of the SED (two sources of the sample). For the same reason, additional components, such as the cold absorber detached from the torus (i.e. Polletta et al. 2008), which might improve the fit but would increase the complexity of the overall modelling, is not included. To reproduce the starburst component, a set of semi-empirical models of well known and studied starburst galaxies is used, as in V09.

4.3. SED fitting procedure

The quality of the fitting solutions is measured using a standard χ^2 minimization technique (as in Hatziminaoglou et al. 2008), where the observed values are the photometric flux densities (from optical-to-MIR/FIR) and the model values are the "synthetic" flux densities obtained by convolving the sum of stars, AGN, and starburst components through the filter response curves.

Before starting the general fitting procedure, we tested which torus parameters mainly influence the global model SED and are more sensitive to our data sets. Parameters that are not constrained by our data were then frozen.

The F06 torus model is described by six parameters: the ratio R_{max}/R_{min} between the outer and the inner radii of the torus (the inner radius being defined by the sublimation temperature of the dust grains); the torus full opening angle Θ; the optical depth τ at 9.7 μm ($\tau_{9.7}$); the line of sight θ with respect to the equatorial plane, and two parameters, γ and α, describing the law for the spatial distribution of the dust and gas density ρ inside the torus (Eq. (1)).

In our approach, we leave the following parameters free to vary inside the pre-constructed grid of torus models: the torus full opening angle Θ, the optical depth $\tau_{9.7}$, and the parameter α describing the radial dependence of the density. We fix $R_{max}/R_{min} = 30$, which translates into compact tori of a few tens of parsecs (given that R_{min} is directly connected to the sublimation temperature and to the accretion luminosity of the central BH). Recent high-resolution IR observations support a compact dust distribution in nearby luminous AGN. Using the interferometry at VLTI in the 8–13 μm band, a torus of size ~2–3 pc
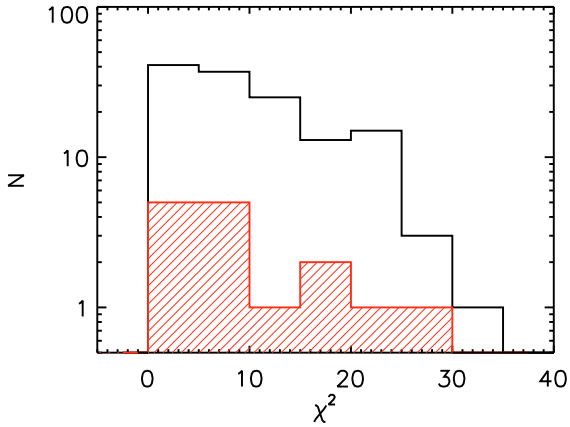
Fig. 2. χ^2 distribution. The red hatched and the empty distributions represent the best-fitting solutions and all the solutions at 1σ, respectively. PKS 0537#43 is not reported given the high χ^2 value (Table 3).

was detected in NGC 1068 (Jaffe et al. 2004). Similar compact tori were also found in other local AGN, such as Circinus and NGC 4151 (see the review by Elitzur 2008).

Regarding the density distribution, we allow power-law profiles that decrease with the radius with different coefficients α. We do not allow any dependence on the distance from the equatorial plane by fixing $\gamma = 0$. As a result, different angles for the lines of sight θ (with respect to the equatorial plane) give the same SED, once the torus is intercepted.

Given the F06 grid of models, the discrete values, allowed for our free parameters, are $\Theta = [60, 100, 140°]$, $\tau_{9.7} = [0.1, 0.3, 0.6, 1, 2, 3, 6, 10]$ and $\alpha = [-1, -0.5, 0]$, implying 72 different torus SEDs.

Considering the stellar component, we fix the redshift for the formation of the oldest SSP at $z = 4$; i.e., given the observed redshift of the sources, we consider galaxies with ages typical of early-type galaxies ($\gtrsim 1$–2 Gyr). This assumption is justified by the observed $R - K_s$ colours and the brightness profiles typical of early-type galaxies as obtained by a detailed morphological analysis in the K_s-band (Mignoli et al. 2004). Concerning the star-formation history, we allow the τ_{sf} parameter of the Schmidt-like law and the value of the extinction $E(B - V)$ to vary. The latter is a key parameter, along with the optical depth $\tau_{9.7}$ of the torus, in shaping the optical-NIR continuum.

Overall, the SED-fitting procedure ends with 5 free parameters (6 when a starburst component is included). Since the problem is affected by some degeneracy, we consider, along with the best-fitting solutions, all the acceptable solutions within 1σ confidence level by considering, for each source, all the solutions with $\chi^2 - \chi^2_{min} = \Delta\chi^2 \lesssim 5.89$ or 7.04, when the cold starburst component is added (see Lampton et al. 1976).

5. Results from SED fitting

In Fig. 2 we show the χ^2 distribution. The hatched histogram represents the distribution of the best-fitting solutions for our 16 targets, while the empty histogram shows the χ^2 distribution of all the solutions within 1σ, satisfying the criteria $\chi^2 \lesssim \chi^2_{min} + \Delta\chi$. Given our adopted grid for the fitted parameters, the total number of solutions at 1σ (constructed by adding all the solutions at 1σ of each object) is 137, or 8 solutions on average per source (including the best-fitting one).

The two distributions do not show a significant difference, and this reinforces our choice of considering all the solutions at

1σ as a unique statistical sample in the analysis of the parameter space and degeneracy.

In terms of the absolute values of the χ^2, only 7 sources (out of 16) give a formally acceptable fit ($P(\chi^2 > \chi^2_{obs}) > 90\%$, see Table 3); the remaining sources have a best-fit model with large χ^2_{obs}. While we use the χ^2 to assign a relative goodness of different parameter combinations inside the parameter grid, we will not take the absolute probabilities at face value. Overestimated χ^2 is, in fact, a common problem of most SED-fitting techniques, resulting from a combination of two different reasons: the limited grid of models (72 torus models with the adopted choice of parameters, see Sect. 4.3) with no uncertainties associated, and the photometric measurements with often underestimated uncertainties (see Gruppioni et al. 2008, for a detailed description of this issue).

In Fig. 3a,b the observed SEDs, from the R-band to the IR (or sub-mm), are reported with the best-fitting models overplotted. All the sources need a host galaxy component and an AGN one. The stellar component dominates in the R and K_s bands, while the nuclear one does at 24 μm. In the IRAC bands, both components contribute, with the fraction depending on the properties of the individual sources. For PKS 0537_43 and G158_19, where data points are available at longer wavelengths, an additional starburst component is needed (Fig. 3b).

In Fig. 4, the relative contributions of the thermal, direct, and scattered light to the total AGN light are shown for two sources characterized by a low ($\tau_{9.7} = 0.1$, PKS 0537#123) and a high ($\tau_{9.7} = 10$, PKS 0537#111) optical depth. While for $\tau_{9.7} = 10$, the AGN emission is dominated by the reprocessed emission in all the UV/optical/IR bands, for $\tau_{9.7} = 0.1$ the direct and scattered components account for the optical/UV AGN emission. Nevertheless, the contribution of the components mentioned above never exceeds the 20% of the observed flux in the R-band. For a sample of highly polarized red AGN selected from the 2MASS survey, a larger contribution of the scattered nuclear component to the optical and near-IR emission was found (Cutri et al. 2002; Kuraszkiewicz et al. 2009). The different result obtained from our analysis is probably due to the different degrees of obscuration of the two samples: the 2MASS sample is characterized by column densities around 10^{22} cm^{-2}, while the present sample has a median column density of 7×10^{22} cm^{-2}.

The negligible contribution of the AGN component, relative to the stellar one, at short wavelengths, is consistent with the upper limits to the AGN emission derived by Mignoli et al. (2004) from the analysis of the K_s-band images (shown as downward-pointing arrows in Figs. 3 and 4). In Table 3, the χ^2 values (and the corresponding degree of freedom) of the best-fitting solutions are reported for each source.

5.1. Torus parameters

In the following section, we discuss how the model torus parameters are constrained by our data set. As anticipated, we consider all the 137 solutions at the 1σ level. First of all, the torus is seen almost edge-on in all the solutions (i.e., the line of sight always intercepts the obscuring material), in agreement with the type 2 X-ray and optical classification of our sources.

The torus model parameters that are left free to vary within the grid of models are the torus opening angle Θ, the slope α of the dust density profile, and the optical depth $\tau_{9.7}$. By converting the torus opening angle into a covering factor (CF) representing the fraction of solid angle covered by the dusty material, we find that solutions with high and low CF are possible, with a slight

Table 3. Best-fitting physical parameters and inferred rest-frame properties.

Abbreviation	χ^2_{min}/d.o.f[a]	α[b]	$\tau_{9.7\,\mu m}$[c]	Θ[d]	τ_{sf}[e]	$E(B-V)$[f]	L_{acc}[g]	$L^h_{1-1000\,\mu m}$	$L_{2-10\,keV}$[i]	$L_{1.25-500\,keV}$[l]	L_{bol}[m]	$k_{2-10\,keV}$[n]	M_{star}[o]	M_{BH}[p]	λ_{Edd}[q]
PKS 0537#43	66.7/6	−1.0	0.1	140	0.05	0.3	373.6	254	6.8	26.3	400 [400–422]	58.8	49.4	10.05	0.032
PKS 0537#11	7.8/5	0.0	2.0	140	0.7	0.64	17.6	7.4	1.9	7.6	25.2 [14.1–34.4]	12.9	1.20	0.28	0.070
PKS 0537#164	9.0/5	0.0	3.0	60	0.15	0.0	99.8	4.9	3.1	12.1	112 [63.0–174]	36.1	1.29	0.30	0.292
PKS 0537#123	5.0/5	0.0	0.1	140	1.0	0.65	9.5	7.8	2.0	7.8	17.3 [17.3–36.4]	8.6	1.99	0.46	0.030
GD 158#62	9.3/5	0.0	0.1	100	0.35	0.44	85.1	39.7	4.9	19.0	104 [67.3–214]	21.2	2.19	0.51	0.163
GD 158#19	26.9/6	0.0	0.3	140	1.0	0.49	397.	289.7	6.3	24.4	422 [422–465]	67.0	12.3	2.64	0.127
Mrk 509#01	17.9/5	−0.5	6.0	60	0.9	0.85	104.5	1.59	1.5	5.8	111 [42.8–131]	73.6	1.98	0.46	0.191
Mrk 509#13	25.0/5	0.0	1.0	140	0.6	1.0	23.2	13.0	2.6	10.1	33.3 [27.1–53.9]	12.8	1.93	0.45	0.059
Abell 2690#75	17.5/5	0.0	1.0	140	0.05	0.18	19.8	11.0	3.2	12.4	32.2 [20.8–66.8]	10.1	2.73	0.62	0.041
PKS 0312#36	9.6/5	0.0	0.1	140	0.85	0.79	3.0	2.5	0.7	2.7	5.7 [5.7–8.1]	8.2	0.43	0.11	0.043
PKS 0537#91	2.9/5	0.0	3.0	140	0.25	0.3	66.0	23.7	8.1	31.4	98.3 [40.2–326]	12.1	1.48	0.35	0.224
PKS 0537#54	2.9/5	0.0	0.1	140	0.05	0.17	5.6	4.6	2.0	7.8	13.3 [13.3–25.8]	6.7	1.72	0.40	0.026
PKS 0537#111	11.4/5	−0.5	10.0	140	0.05	0.31	103.1	13.4	1.7	6.6	110 [34.1–110]	64.4	4.61	1.03	0.084
Abell 2690#29	0.5/2	0.0	1.0	140	0.15	0.55	168.8	94.7	8.4	32.6	201 [135–264]	23.9	17.9	3.80	0.042
PKS 0312#45	0.5/5	0.0	0.1	100	0.25	0.48	24.25	11.3	6.2	24.0	48.3 [37.4–239]	7.8	3.61	0.81	0.047
BPM 16274#69	0.5/5	0.0	0.6	140	0.05	0.25	11.4	7.3	2.4	9.3	20.7 [18.2–56.6]	8.6	4.68	1.05	0.016

Notes. [a] Best-fitting minimum χ^2 and number of degrees of freedom; [b–d] best-fitting torus parameters (α: exponent of the power law parameterizing the density profile; $\tau_{9.7\,\mu m}$: 9.7 μm optical depth, Θ: torus opening angle). The ratio parameter R_{max}/R_{min} is frozen to 30; the density parameter γ is frozen to 0; [e, f] best-fitting stellar parameters (τ_{sf}: duration of the exponential decay of the burst in units of the oldest SSP; $E(B-V)$: extinction); [g] accretion-disk model luminosity (from soft X-ray to IR frequencies) which represents the torus model input luminosity, in units of 10^{44} erg s^{-1}; [h] torus luminosity in units of 10^{44} erg s^{-1} (not corrected, see Sect. 6.1); [i] absorption-corrected luminosity in units of 10^{44} erg s^{-1}; [l] hard-X-ray luminosity in units of 10^{44} erg s^{-1} (derived from the 2–10 keV luminosity, see Sect. 6.2); [m] bolometric AGN luminosity ($L_{acc} + L_{1.25-500\,keV}$) in units of 10^{44} erg s^{-1}; the 1σ range derived from the SED-fitting analysis is reported; [n] 2–10 keV bolometric correction ($L_{bol}/L_{2-10\,keV}$); [o] galaxy masses in units of 10^{11} $M_\odot$; [p] black hole masses in units of 10^9 $M_\odot$ (estimated from Marconi & Hunt 2003, relation); [q] Eddington ratios (L_{bol}/L_{Edd}).

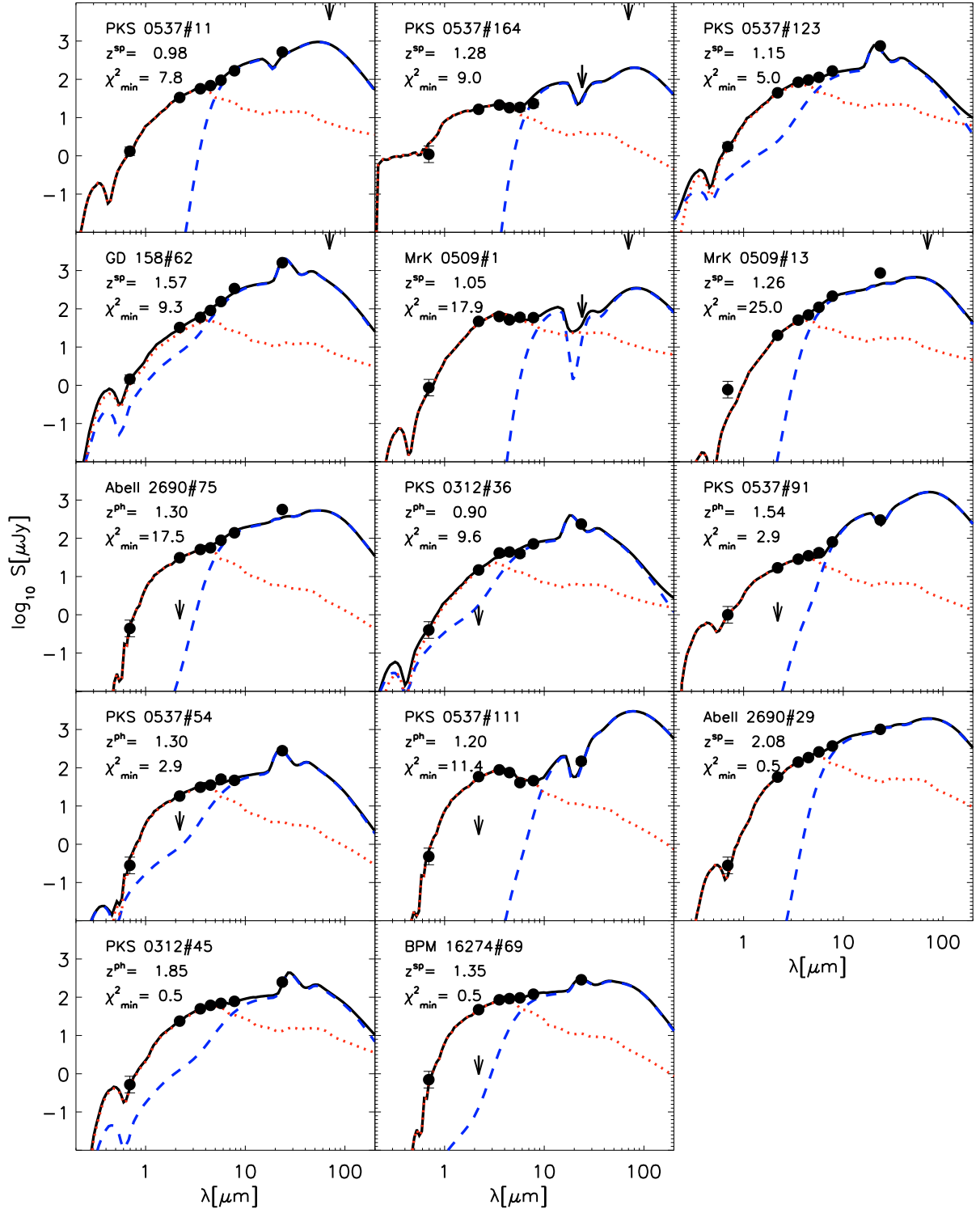**Fig. 3. a)** Observed-frame SEDs for 14 sources with data from the R-band to the 24 μm (black dots) compared with the best-fit model obtained as the sum (solid black line) of a stellar component (red dotted line) and an AGN component (blue dashed line). The nuclear K_s-band upper limits (downward-pointing arrows) were derived from the morphological analysis carried out by Mignoli et al. (2004).

preference for tori with large CF. The mean CF value is 0.65 ($1\sigma \sim 0.25$), corresponding to a torus opening angle of $\sim 110°$.

According to Maiolino et al. (2007), the covering factor of the circum-nuclear dust decreases for increasing optical luminosity at 5100 Å (L_{5100}). This relation is explained in terms of a "receding-torus". In Maiolino et al. (2007) the luminosities at

5100 Å were derived from optical spectroscopy and the CF values from the ratios between the 6.7 μm and the 5100 Å luminosities for a sample of type 1 quasars spanning five orders of magnitude in optical luminosity. In our approach, L_{5100} is estimated for each solution from the input accretion-disk spectrum (see Sect. 4.1), once the normalization is found (see Sect. 6.1). The average value of CF and L_{5100} for our sample lies within 1σ
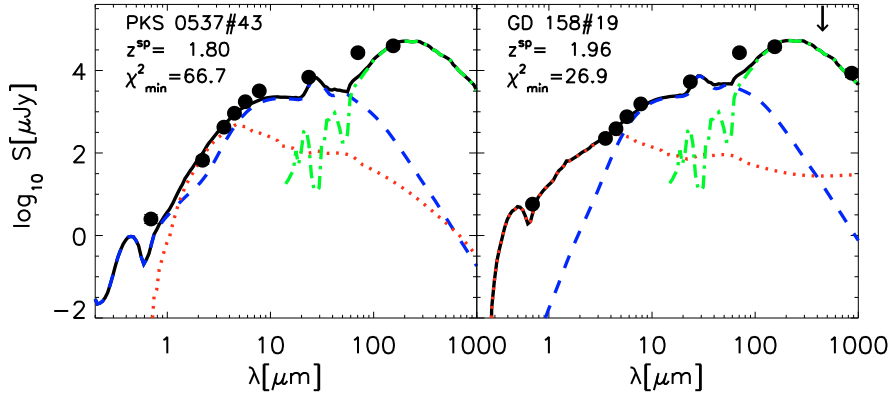
Fig. 3. b) As in Fig. 3a for sources with detections also at longer wavelengths (FIR/sub-mm). An additional starburst component (green dot-dashed line) is considered in the best-fit model.
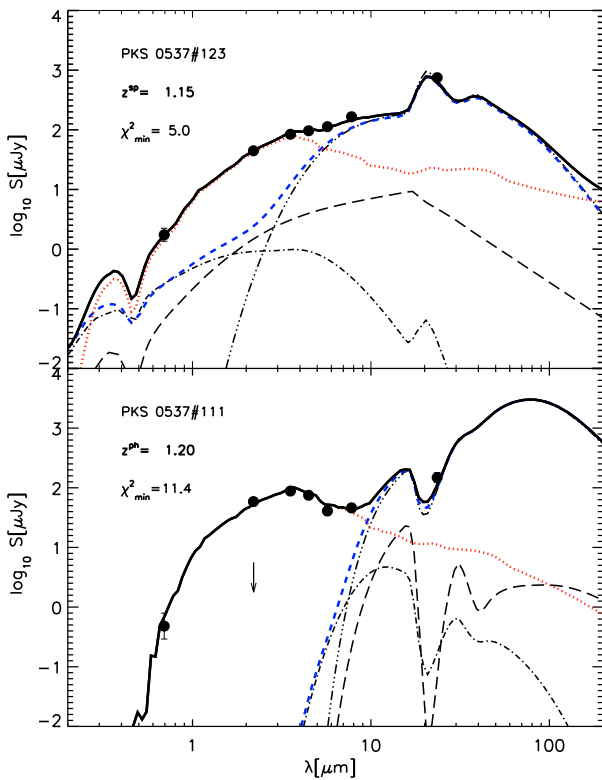

Fig. 4. Observed-frame spectral energy distribution as in Figs. 3a,b for 2 sources characterized by extreme values of the optical depth: $\tau_{9.7\,\mu m} = 0.1$ for PKS 0537_123 and 10 for PKS 0537_111. In this figure, the 3 different components that contribute to the AGN emission are reported: direct nuclear light (long-dashed line), scattered light (dashed-dot line), and thermally re-emitted light (dashed-dot-dot-dot line).

Fig. 5. *Top panel*: the fraction of solutions with flat density profile ($\alpha = 0$) as a function of $\tau_{9.7}$. *Bottom panel*: the $\tau_{9.7}$ distribution. The hatched and the empty distributions represent the best-fitting (16) and all the solutions (137) at 1σ, respectively.

on the relation found by Maiolino et al. (2007). Unfortunately, given the limited range of L_{5100}, we cannot investigate the validity of the CF vs. L_{5100} relation over the range probed by Maiolino et al. (2007).

Regarding the density profile, about 65% of the solutions have $\alpha = 0$, while $\alpha = -0.5$ and $\alpha = -1.0$ represent 20% and 15% of the solutions, respectively. This is also reflected in the 16 best-fitting solutions, where only 2 sources (Mrk 0509#1 and PKS 0537#111) are fitted with $\alpha = -0.5$, one with $\alpha = -1.0$ (PKS 0537#43) and the remaining ones with $\alpha = 0$ (see Table 3).

Solutions with a moderate optical depth $\tau_{9.7}$ are favoured by the SED-fitting analysis. As shown in Fig. 5 (*bottom* panel), there are few solutions with high optical depths while the
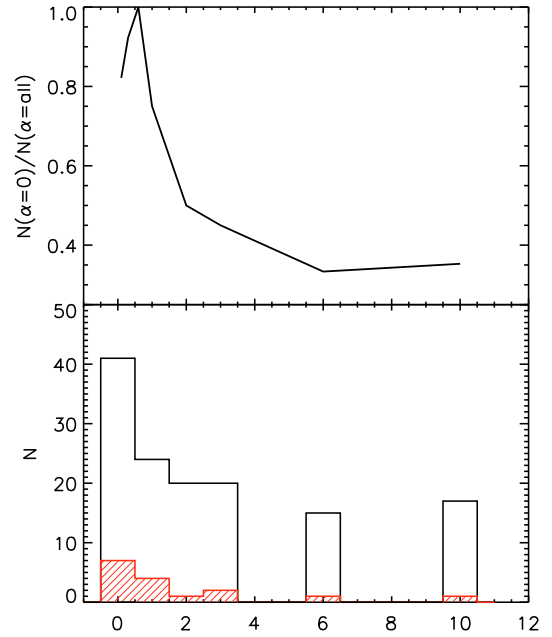
majority of the solutions (~80%) are characterized by "moderate" $\tau_{9.7}$ ($\tau_{9.7} \leq 3$) and 50% by low ($\tau_{9.7} \leq 1$). The median value for $\tau_{9.7}$ is 2.

The finding of a preferred range of optical depths by the SED-fitting, even with relatively sparse photometric data, comes from the overall shape of the NIR/MIR continuum. In fact, once the stellar component is determined by the optical/NIR data, the slope of the torus component is directly linked to the amount of absorption (i.e., to the optical depth) and is relatively well constrained by the available data. As shown in Fig. 3a,b, for the very low values of the optical depth $\tau_{9.7}$ ($\tau_{9.7} = 0.1$), the F06 model predicts spectra with a weak emission line at $9.7\,\mu m$.

We clearly find that the optical depth $\tau_{9.7}$ and the density profile α are not independent parameters, since low optical depth solutions mostly occur with flat density profile ($\alpha = 0$). This is shown in Fig. 5 (*top* panel), where the fraction of solutions with $\alpha = 0$ is reported as a function of $\tau_{9.7}$. For the assumed flared disk geometry, at high optical depth a flat density profile produces too much IR emission because of the large amount of dust at high radii. Thus the two best-fitting solutions with the highest

$\tau_{9.7}$ found ($\tau_{9.7} = 6$ and 10 for Mrk 509#01 and PKS 0537#111 respectively, see Fig. 5 and Table 3) have a density profile decreasing with the distance from the central BH ($\alpha = -0.5$).

Recalling that in our procedure different lines of sight are equivalent (having assumed $\gamma = 0$ in the radial density profile, Eq. (1)), we can convert the optical depths to column densities $N_{\rm H}$ (adopting a Galactic dust-to-gas ratio) to be compared with the $N_{\rm H}$ derived from the X-ray observations. Despite the uncertainties affecting the derivation of $N_{\rm H}$ from the dust's optical depths (i.e., dust and gas spatial distributions could be different), as well as those affecting the $N_{\rm H}$ values from X-rays (see Perola et al. 2004, for details and Table 1), the two independent estimates give a consistent picture for the majority of the sources, once the 1σ uncertainties derived from the SED and X-ray fitting procedure are taken into account. By excluding the two sources without a measured $N_{\rm H}$ from the X-rays analysis (see Table 1), the median values for $N_{\rm H}$ are $\sim 7 \times 10^{22}$ cm^{-2} from the X-rays analysis and $\sim 5.5 \times 10^{22}$ cm^{-2} from the dust optical depths. Therefore, the SED-fitting method confirms the X-ray classification of the sources as moderately obscured Compton-thin AGN.

Two sources have a significantly different $N_{\rm H}$ (by an order of magnitude) derived with the two methods, PKS 0537#111 and Mrk 509#01. These objects are those characterized by the highest optical depths ($\tau_{9.7} = 6, 10$, which are converted into $N_{\rm H} \sim 5.3 \times 10^{23}$ cm^{-2} and $N_{\rm H} \sim 8.7 \times 10^{23}$ cm^{-2}, respectively). Since Mrk 509#01 only has an upper limit for the $N_{\rm H}$ inferred from X-ray analysis ($< 1.1 \times 10^{22}$ cm^{-2}, see Table 1), the observed discrepancy for this object might be explained if the source is Compton-thick ($N_{\rm H} \geq 10^{24}$ cm^{-2}), and the observed X-ray spectrum is due to a reflection component. However, we cannot draw any firm conclusion on this issue.

5.2. Host galaxy parameters

In the spectral procedure, the host galaxy accounts for the optical/near-IR photometric data points, where the AGN contribution is presumably low, given the obscured nature of our sources. We use the SSP spectra weighted by a Schmidt-like law of star formation (see Sect. 4.2). The extinction $E(B-V)$ and $\tau_{\rm sf}$ are free parameters. Once the best-fitting values for these two parameters are found, the stellar mass (obtained by integrating the star formation history over the galaxy age and subtracting the fraction due to mass loss during stellar evolution, $\sim 30\%$, from it) is estimated from the SED normalization. At the end of the SED fitting procedure, stellar masses are well-constrained, for a given pair of $E(B-V)$ and $\tau_{\rm sf}$, with a typical 1σ uncertainty for the normalization of $\sim 20\%$.

All but one of the stellar masses derived in this work are within 30% from the values estimated by Pozzi et al. (2007; eight sources in common), where the same data were used but different stellar libraries and a simpler approach was adopted (see Sects. 4.1 and 5.2 of Pozzi et al. 2007).

The stellar masses found are in the range 4×10^{10} up to $5 \times 10^{12}\ M_\odot$ with three very massive galaxies ($> 10^{12}\ M_\odot$, see Table 3), implying that our obscured AGN are hosted by massive galaxies at high redshift. As said in Sect. 4.2, the masses are obtained using a Salpeter (1955) initial mass function (IMF) with mass in the range (0.15–$120\ M_\odot$). The assumption of a Chabrier (2003) IMF (see Renzini 2006) would produce a factor of ~ 1.7 lower stellar masses.

In Table 3, the best-fitting value for the free host galaxy parameters ($\tau_{\rm sf}$ and $E(B-V)$), and the stellar masses are reported for each source.

6. Black hole physical properties

6.1. Black hole accretion luminosities

The accretion-disk luminosity $L_{\rm acc}$ is a direct output of the fitting procedure and is obtained by integrating the code input energy spectrum once the best-fitting torus components and its normalization are found (see Sect. 4.3).

The input spectrum is defined in the 10^{-3} to $20\ \mu$m regime. Although this wavelength range provides the largest contribution to the nuclear AGN luminosity, we also included the hard X-ray luminosity ($L_{1.25-500\ {\rm keV}}$) in the $L_{\rm acc}$ computation. This luminosity is estimated from the de-absorbed, k-corrected $L_{2-10\ {\rm keV}}$ luminosity, assuming a photon index $\Gamma = 1.9$ (typical of AGN emission) and an exponential cut-off at 200 keV (e.g., Gilli et al. 2007). A different choice for the energy cut-off (e.g., at 100 keV) would produce a difference by $\approx 20\%$ in the total X-ray luminosity for $\Gamma = 1.9$ sources (see Vasudevan et al. 2010). Dust grains are almost transparent to hard X-ray photons, therefore the output of the code is not affected by the accretion-disk model spectrum not extending above soft-X-ray energies.

In Table 3 $L_{\rm bol}$, along with $L_{\rm acc}$ and $L_{1.25-500\ {\rm keV}}$, are reported. $L_{\rm bol}$ extends over two orders of magnitudes (10^{44}–10^{46} erg s^{-1}), with the hard-X-ray luminosities (1.25–500 keV) contributing to the AGN power in the range 5–50% (see Table 3). The two sources with the highest optical depths ($\tau_{9.7\ \mu m} = 6, 10$) are among the sources with the smallest hard-X-ray fraction (Mrk 509#01 and PKS 0537#111). In Table 3 we also report the range of bolometric luminosities as obtained by considering the full set of 1σ solutions. The uncertainties are, on average, about 0.2 dex, but vary significantly from source to source, ranging from about 5% to about a factor 3 (see also Fig. 7).

We compare the computed bolometric luminosities with the luminosities derived by integrating the torus best-fitting templates from 0.1–1000 μm (plus adding the hard X-ray luminosity for self-consistency). The two methods assume the same torus SED, so the comparison can give important information on the systematics affecting the estimates of $L_{\rm bol}$ derived by integrating the observed SED, which is the widely used method. We refer to the first measures as the "model" luminosities and to the second as the "observed" luminosities.

The "observed" $L_{\rm bol}$ (see Fig. 6) are lower (up to an order of magnitude) than the "model" ones for all the solutions and the median value of the ratio is $R \sim 2$. An underestimate of the luminosity in type 2 sources is expected by torus models (e.g., Pier & Krolik 1993; Granato & Danese 1994); here, we quantify this effect and provide an empirical factor to correct the 'observed' luminosities, at least for this class of sources.

We underline how the observed discrepancy does not depend on the lack of observations at far-IR wavelengths. In fact, the two methods assume the same torus SED for self-consistency (i.e., the integrated torus SED to estimate the observed IR luminosity is the output of the code); under this hypothesis, an over(under)-estimate on one luminosity would introduce the same effect on the other. As a result, a poor sampling in the far-IR would have the same impact on both (i.e. "observed" and "model") luminosities. Our analysis takes this uncertainty into account by considering all the solutions (i.e., all torus models) at the 1σ confidence level. By means of this procedure, a broad range of model SED is associated to each source (on average, eight solutions; see Sect. 5), characterized by different emission in the mid/far-IR region, as a result of different torus geometry and absorption properties (see Fig. 3).

As explained in Pier & Krolik (1992), the low values of the "observed" $L_{\rm bol}$ depend on a combination of three factors: the
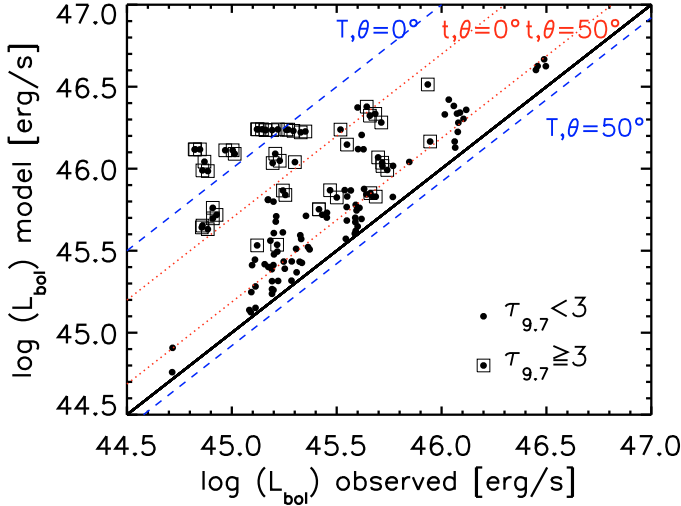
Fig. 6. "Model" as a function of "observed" bolometric luminosities for the sample of luminous obscured quasars at the 1σ significance level (137 solutions). Squares around the filled circles represent the solutions with high optical depth ($\tau_{9.7\,\mu m} \geq 3$). The "observed" bolometric luminosities are reported with no corrections applied. The solid line represents the identity relation. The dotted and dashed lines represent the predictions from the Pier & Krolik (1992) model for 4 different configurations for type 2 sources as a function of the optical depths τ_z and τ_r (where τ_z and τ_r are the optical depths at 9.7 μm along the vertical- with respect to the torus equatorial plane – and the radial direction, respectively) and viewing angle θ (with respect to the equatorial plane). Red dotted lines: thinner model ($\tau_z = \tau_r = 0.1$, labelled with the letter t) with $\theta = 0, 50°$. Blue dashed lines: thicker model ($\tau_z = 1$, $\tau_r = 10$, labelled with the letter T) with $\theta = 0, 50°$. At constant optical depth, the configurations with smaller viewing angles (closer to the equatorial torus plane) predict lower "observed" luminosities.

torus opening angle Θ (geometrical factor), the observer viewing angle θ, and the torus optical thickness $\tau_{9.7\,\mu m}$. By erroneously assuming isotropic torus emission (done to compute the "observed" L_{bol}), the primary flux that does not intercept the obscuring material would not be included in the luminosity budget; moreover, as the thickness of the torus increases, more and more primary high-energy photons entering the torus are absorbed by the dust grains and re-emitted isotropically (hence also in directions escaping the torus it self). This effect is explained by the *dust self-absorption*, i.e., thermal dust emission absorbed by the dust itself. For high optical depth, the outer edges of the torus absorb the IR photons coming from the warmer dust at smaller radii and re-emit them isotropically, i.e., also in directions outside the line of sight. To better visualize this effect, we report in Fig. 6 the "observed" versus "model" luminosities, as predicted by Pier & Krolik (1992), as a function of the viewing angle θ and the torus optical thickness $\tau_{9.7\,\mu m}$ for 4 sets of type 2 configurations (as described in the caption). Although there are some slight differences between the F06 model (adopted here) and the Pier & Krolik (1992) torus model (where the optical depth varies independently along the radial and the vertical axis), optically thinner models show less anisotropy (red dotted lines in Fig. 6, corresponding to two different viewing angles), than higher $\tau_{9.7\,\mu m}$ models (blue dashed lines in Fig. 6, corresponding to the same viewing angles considered for the thinner model). The cold outer edges of the thicker models, in fact, radiate little and block the light coming from the inner torus radii.

To investigate these issues further, we apply a "conservative" correction to our "observed" luminosities, meant to correct
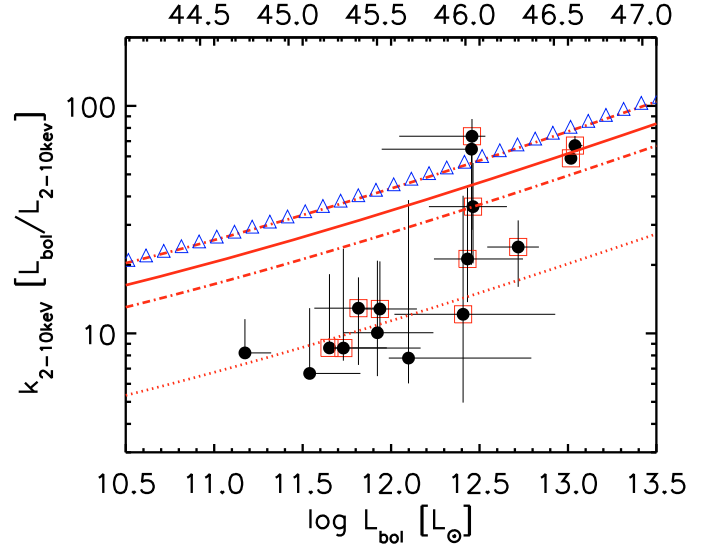

Fig. 7. 2–10 keV bolometric corrections as a function of the "model" bolometric luminosities (filled circles). Filled circles inside empty red squares represent the sources with a spectroscopic redshift. The red solid and dot-dashed lines represent the predictions from the Marconi et al. (2004) relation and its 1σ dispersions. Also, the expectations from Hopkins et al. (2007) are reported as empty blue triangles. The red dotted line represents the Marconi et al. (2004) expectations at 5σ from the best-fitting relation.

only for the geometrical factor; in other words, we divided each "observed" luminosity by the corresponding covering factor CF ($\sim$0.58 for $\sim$100° and $\sim$0.88 for $\sim$140°). Although this correction increases the "observed" luminosities, the "model" ones are still higher ($R \sim 1.6$). The remaining discrepancy is mostly found for solutions with high optical depth, as expected ($R \sim 5$ for models with $\tau_{9.7} \geq 3$; see Fig. 6, where the squares mark the 52 solutions with $\tau_{9.7} \geq 3$).

An independent and consistent analysis was also done by Pozzi et al. (2007, see their Sect. 5.1) where a first-order correction of $\sim$2 to the "observed" luminosities was estimated, accounting for geometrical and anisotropy effects; in that work, however, the correction was estimated using the ratio of obscured/unobscured quasars according to the Gilli et al. (2007) AGN synthesis models of the X-ray background and the different shape of type 2 vs. type 1 quasar SEDs as a function of the column density. In Pozzi et al. (2007), the SED fitting was done using the Silva et al. (2004) AGN templates. Since the template choice was based on the X-ray N_H (and not on the N_H resulting from the torus modelling as in the present analysis), the correction corresponding to the thicker models ($N_H \gtrsim 10^{24}$ cm^{-2}) was not included since no Compton-thick objects were revealed in X-rays.

6.2. Hard X-ray bolometric corrections

In Fig. 7 the bolometric-to-X-ray luminosity ratio ($k_{2-10\,keV}$) is shown as a function of L_{bol}. For the bolometric luminosities we assume the model ones. The error bars on $k_{2-10\,keV}$ are derived from the 1σ dispersion on L_{bol}.

A wide spread in the $k_{2-10\,keV}$ is found ($6 \lesssim k_{2-10\,keV} \lesssim 80$), as also pointed out by the pioneering work of Elvis et al. (1994) on type 1 QSOs, owing to the large dispersion in the AGN spectral shape. Our median value ($k_{2-10\,keV} \sim 20$, estimated from the 137 solutions) is marginally consistent with the mean value

of Elvis et al. (1994), ~25 after removing the IR contribution (in order not to double-count the fraction of the nuclear emission absorbed by the circumnuclear dusty material seen almost face-on). We confirm the trend to higher $k_{2-10\,\mathrm{keV}}$ for objects with higher bolometric luminosities as predicted by Marconi et al. (2004; see Fig. 7) but our $k_{2-10\,\mathrm{keV}}$ values are significantly lower (at least a factor 2 in normalization). They derive $k_{2-10\,\mathrm{keV}}$ by constructing an AGN reference template taking into account how the spectral index α_{ox} varies as a function of the luminosity (Vignali et al. 2003). Predictions consistent with Marconi et al. (2004) have been obtained more recently by Hopkins et al. (2007, Fig. 7), considering the most recent determination of SED templates (i.e. Richards et al. 2006) and α_{ox} (i.e. Steffen et al. 2006).

Our low values for $k_{2-10\,\mathrm{keV}}$ are consistent with our previous analysis (median $k_{2-10\,\mathrm{keV}} \sim 25$, Pozzi et al. 2007) based on a different method and on different AGN templates (Silva et al. 2004) and with other estimates found in literature for hard X-ray-selected samples. Kuraszkiewicz et al. (2003) considered a sample of X-ray-selected luminous AGN ($10^{43} < L_{2-10\,\mathrm{keV}} < 10^{46}$ erg s^{-1}) and find a median $k_{2-10\,\mathrm{keV}}$ of 18. Ballo et al. (2007), analysed a sample of low-luminosity AGN ($10^{42} < L_{2-10\,\mathrm{keV}} < 10^{43.6}$ erg s^{-1}) and find a median $k_{2-10\,\mathrm{keV}}$ of 12. Low bolometric-to-X-ray ratios, consistent with our estimate (median $k_{2-10\,\mathrm{keV}} \sim 25$, $1\sigma = 53$) have been found recently by Lusso et al. (2010), where the statistical properties of a large (and complete) sample of 545 X-ray-selected type 1 QSO from the XMM-COSMOS survey (Hasinger et al. 2007) are presented.

The lower bolometric-to-X-ray luminosity ratios found in the present work (and in the above mentioned samples), in comparison to the Marconi et al. (2004) and Hopkins et al. (2007) predictions, are probably caused by a selection bias, since our sample (and most of the above cited ones) are hard X-ray-selected samples (i.e., sources with high X-ray luminosity are favoured). Moreover, as discussed in Sect. 2, our sources are among the most extreme X-ray sources, being characterized by red optical-to-NIR colours ($R - K_s \gtrsim 5$) and high X-ray-to-optical ratio (X/O $\gtrsim 1$). Our selection is very likely the origin of the large deviation (at about the 5σ level) for a large fraction of the present sample (see Fig. 7) from the Marconi et al. (2004) relation. To further explore this issue, a larger (and complete) sample of X-ray sources (with optical identification up to the faintest X-ray fluxes) is needed, in order to correct for the selection bias and to derive the properties of the parent AGN population (see Lusso et al. 2010).

6.3. Black hole masses

The BH masses are not a direct output of the best-fitting procedure and cannot be derived with "standard methods" (i.e. galaxy stellar kinematics, nuclear gas motions, reverberation). We estimate them indirectly using the $M_{\mathrm{bulge}} - M_{\mathrm{BH}}$ relation derived locally by Marconi & Hunt (2003) and by assuming as M_{bulge} the stellar mass derived from our best-fitting procedure. The main uncertainties affecting these estimates derive from the extrapolation of the local relation to higher z, where the behaviour of this relation is still a matter of debate (see discussion in Pozzi et al. 2007). The stellar masses are constrained quite well by the SED-fitting procedure inside the pre-constructed grid of galaxy models (see Sect. 5.2).

The inferred black hole masses are typically in the range $10^8 - 10^9 M_\odot$, with three sources (PKS 0537#43, GD 158#19, Abell 2690#29) with higher masses ($M_{\mathrm{BH}} \sim 10^{9.5} - 10^{10.0} M_\odot$). The range of BH masses is consistent with the values reported
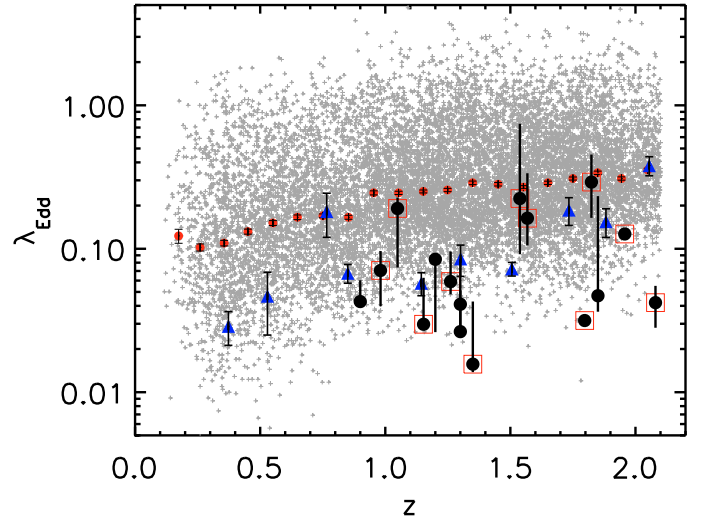
Fig. 8. λ_{Edd} as a function of z. Black circles: sources of the present sample. Red squares as in Fig. 7. The error bars represent the 1σ uncertainties on L_{bol} (as derived from the χ^2 analysis). Small grey crosses: sample of SDSS quasars from McLure & Dunlop (2004), with the median values (and associated uncertainties assuming the normalized median absolute values) of λ_{Edd} within $\Delta z = 0.1$ bins shown as red filled circles. Blue triangles: median values (and associated uncertainties assuming the normalized median absolute values) of λ_{Edd} within $\Delta z = 0.2$ bins from the COSMOS type 1 sample of Lusso et al. (2010).

by McLure & Dunlop (2004) for the SDSS quasars in the same redshift interval ($0.9 \lesssim z \lesssim 2.1$, see also Shen et al. 2008, where new BH masses are derived).

In Fig. 8, the Eddington ratios λ_{Edd}, defined as $\lambda_{\mathrm{Edd}} = L_{\mathrm{bol}}/L_{\mathrm{Edd}}$ (with $L_{\mathrm{Edd}} = 1.38 \times 10^{38} M_{\mathrm{BH}}/M_\odot$), are reported as a function of redshift. The values are compared with those of the whole SDSS quasar sample (McLure & Dunlop 2004) and those obtained by Lusso et al. (2010) for the subsample of 150 X-ray selected type 1 AGN in COSMOS with an accurate black hole mass determination.

The λ_{Edd} values of the present work cover slightly more than an order of magnitude (0.01–0.3) with a median value of $\lambda_{\mathrm{Edd}} \sim 0.08$ (estimated considering all the 137 solutions at 1σ level, see Sect. 5). The derived values are within the 3σ confidence interval of the SDSS quasar λ_{Edd} distribution, characterized by a median value of ~0.3 and with a dispersion of 0.35 dex at the same redshift interval sampled by our sources. However, almost all our data points lie towards the low λ_{Edd} tail of the SDSS distribution (see Fig. 8), suggesting that X-ray selection is biased towards slightly lower λ_{Edd} than optical selection. Our data are fully consistent with the results obtained from a much larger sample of X-ray-selected type 1 AGN in the COSMOS field (Lusso et al. 2010).

The results are robust against the uncertainties on the extrapolation, discussed above, of the local $M_{\mathrm{bulge}} - M_{\mathrm{BH}}$ relation, at the redshift of our sample. In fact, allowing for positive evolution with redshift of the $M_{\mathrm{BH}}/M_{\mathrm{bulge}}$ ratio by a factor of 2 (e.g., Hopkins et al. 2006; Shields et al. 2006; Merloni et al. 2010), the Eddington ratios λ_{Edd} would decrease further by the same factor.

Finally, in Fig. 9, the bolometric corrections $k_{2-10\,\mathrm{keV}}$ are plotted against the Eddington ratios λ_{Edd} (following Vasudevan & Fabian 2009). The error bars representing the 1σ confidence interval derived from the uncertainties on L_{bol}. Along with our data we show the Vasudevan & Fabian (2009) results, where simultaneous optical, UV and X-ray observations are included for
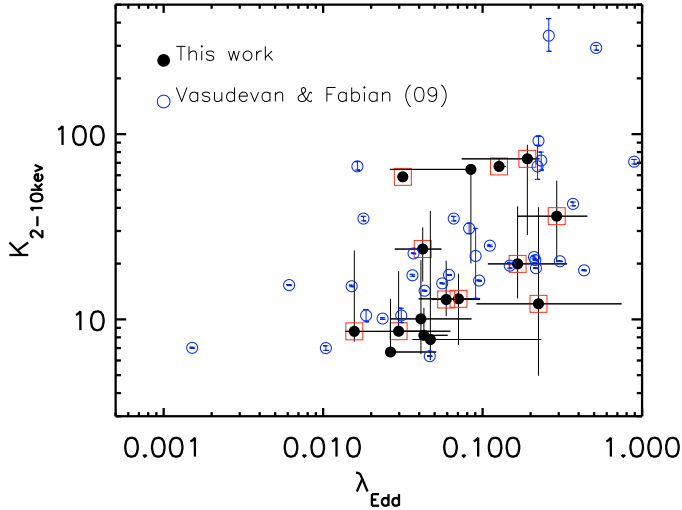
Fig. 9. $k_{2-10\ \text{keV}}$ as a function of λ_{Edd}. Black filled symbols: sources of the present sample. Red squares as in Fig. 7. The error bars represent the 1σ uncertainties on L_{bol} (as derived from the χ^2 analysis), which affect both the $k_{2-10\ \text{keV}}$ and the λ_{Edd} values. Blue open symbols: sources from Vasudevan & Fabian (2009).

the majority of the Peterson et al. (2004) reverberation mapped sample of AGN. Our findings are in fairly good agreement with the trend towards increasing $k_{2-10\ \text{keV}}$ for increasing λ_{Edd}. Vasudevan & Fabian (2009) interpret the observed trend as the result of different black hole SED shape as a function of the Eddington ratio, with the high and low Eddington ratios corresponding to different fractions of the ionizing UV luminosity. A similar trend has been recently found for a sample of 63 type 1 and type 2 AGN detected in the *Swift*/BAT 9-month catalogue (see Vasudevan et al. 2010). At variance with the assumption in Vasudevan & Fabian (2009), where the bolometric luminosities were derived by integration over the observed optical/UV/X-ray SED, in this work the authors consider the reprocessed IR emission, reproduced by the empirical SEDs of Silva et al. (2004), as a proxy of the intrinsic AGN bolometric luminosity, as first suggested by Pozzi et al. (2007).

The dependence of bolometric corrections on Eddington ratios is expected by accretion-disk models, which predict an increasing hard X-ray bolometric corrections at increasing accretion rates (e.g. Witt et al. 1997). Recently also studying a large (156 sources) sample of type 1 X-ray AGN from the XMM-*Newton* archive, Bianchi et al. (2009) suggest that the bolometric correction must depend on the Eddington ratio to allow the intrinsic power of AGN to scale linearly with black hole masses.

7. Summary

We analysed the SEDs of a sample of 16 obscured quasars selected in the hard X-ray band. *Spitzer* mid/far-IR photometry (IRAC and MIPS), along with the data available in the literature, is modelled using a multi-component model, where the AGN re-processed emission is reproduced in the context of a flared disk model, as described by F06. Within the context of a flared disk torus model, the uncertainty in and degeneracy between the various derived parameters are accounted for by including all solutions within 1σ of the best-fit in the subsequent analysis.

The main results are summarized below.

- All the 16 quasars were detected up to 8 μm and all but two sources were detected at 24 μm with flux densities in the range

100–7000 μJy at the 5σ level. The two most luminous sources of the sample were also detected at 70 and 160 μm.
- The observed broad-band spectral energy distributions were reproduced well by a multi-component model comprising a stellar, an AGN, and a starburst component (when far-IR detections were available). The AGN component, modelled with the F06 radiative transfer code, accounts for the X-ray emission and for a fraction of the IR emission, mainly because of reprocessed emission from the putative dusty torus surrounding the central black hole.
- Solutions with a moderate optical depth $\tau_{9.7}$ are favoured by the SED-fitting, with the majority of the sources having moderate optical depths ($\tau_{9.7\ \mu m} \leq 3$). The derived gas column densities (N_{H}) are consistent, for most of the sources, with the values estimated from the X-ray analysis, both indicating that the sources are Compton-thin AGN ($N_{\text{H}} \sim 10^{22} - 3 \times 10^{23}\ \text{cm}^{-2}$).
- The model nuclear bolometric luminosities are in the range $5 \times 10^{44} - 4 \times 10^{46}\ \text{erg s}^{-1}$. By comparing these values with those obtained by integrating the nuclear observed SED, we concluded that the latter underestimates the bolometric luminosities by a factor of 2. The difference may be explained by anisotropic torus emission and the effect of the torus optical depth (e.g., Pier & Krolik 1992).
- From the model nuclear SEDs, we estimated the bolometric-to-X-ray corrections ($k_{2-10\ \text{keV}}$). The median $k_{2-10\ \text{keV}}$ is $\sim$20 ($6 \lesssim k_{2-10\ \text{keV}} \lesssim 80$). The value is lower than assumed by some models of BH evolution ($k_{2-10\ \text{keV}} \gtrsim 40$ at the median luminosity of our sample). The discrepancy is significant at 5σ level at low bolometric luminosity.
- By assuming the local $M_{\text{bulge}} - M_{\text{BH}}$ relation, we estimate λ_{Edd} with a median value of 0.08 ($0.01 \lesssim \lambda_{\text{Edd}} \lesssim 0.3$). The whole SDSS quasar sample, at the same redshift interval sampled by our objects, is characterized by a median value of 0.3. Our data are within the 3σ confidence level of the optically selected quasar distribution; however, almost all our sources lie towards the low λ_{Edd} tail of the SDSS distribution, suggesting that our X-ray selection is biased more towards lower Eddington efficiencies than optical selection.
- The data are consistent with the correlation recently suggested by Vasudevan & Fabian (2007, 2009) between $k_{2-10\ \text{keV}}$ and λ_{Edd}, where low bolometric corrections are found at low Eddington ratios.

References

Agol, E., Gogarten, S. M., Gorjian, V., & Kimball, A. 2009, ApJ, 697, 1010
Baldi, A., Molendi, S., Comastri, A., et al. 2002, ApJ, 564, 190
Ballo, L., Cristiani, S., Fasano, G., et al. 2007, ApJ, 667, 97
Berta, S., Fritz, J., Franceschini, A., Bressan, A., & Lonsdale, C. 2004, A&A, 418, 913
Bianchi, S., Bonilla, N. F., Guainazzi, M., Matt, G., & Ponti, G. 2009, A&A, 501, 915
Brusa, M., Comastri, A., Daddi, E., et al. 2005, A&A, 432, 69

Cardelli, J. A., Clayton, G. C., & Mathis, J. S. 1989, ApJ, 345, 245
Chabrier, G. 2003, PASP, 115, 763
Cocchia, F., Fiore, F., Vignali, C., et al. 2007, A&A, 466, 31
Dullemond, C. P., & van Bemmel, I. M. 2005, A&A, 436, 47
Efstathiou, A., & Rowan-Robinson, M. 1995, MNRAS, 273, 649
Elitzur, M. 2008, New Astron. Rev., 52, 274
Elitzur, M., & Shlosman, I. 2006, ApJ, 648, L101
Elvis, M., Wilkes, B. J., McDowell, J. C., et al. 1994, ApJS, 95, 1
Fabian, A. C. 1999, MNRAS, 308, L39
Fadda, D., Marleau, F. R., Storrie-Lombardi, L. J., et al. 2006, AJ, 131, 2859
Fiore, F., Brusa, M., Cocchia, F., et al. 2003, A&A, 409, 79
Fiore, F., Grazian, A., Santini, P., et al. 2008, ApJ, 672, 94
Frayer, D. T., Huynh, M. T., Chary, R., et al. 2006, ApJ, 647, L9
Frayer, D. T., Sanders, D. B., Surace, J. A., et al. 2009, AJ, 138, 1261
Fritz, J., Franceschini, A., & Hatziminaoglou, E. 2006, MNRAS, 366, 767 (F06)
Gilli, R., Comastri, A., & Hasinger, G. 2007, A&A, 463, 79
Granato, G. L., & Danese, L. 1994, MNRAS, 268, 235
Gruppioni, C., Pozzi, F., Polletta, M., et al. 2008, ApJ, 684, 136
Haardt, F., & Maraschi, L. 1991, ApJ, 380, L51
Hasinger, G., Cappelluti, N., Brunner, H., et al. 2007, ApJS, 172, 29
Hatziminaoglou, E., Fritz, J., Franceschini, A., et al. 2008, MNRAS, 386, 1252
Hatziminaoglou, E., Fritz, J., & Jarrett, T. H. 2009, MNRAS, 1247
Hönig, S. F., Beckert, T., Ohnaka, K., & Weigelt, G. 2006, A&A, 452, 459
Hopkins, P. F., Hernquist, L., Cox, T. J., et al. 2006, ApJS, 163, 1
Hopkins, P. F., Richards, G. T., & Hernquist, L. 2007, ApJ, 654, 731
Jaffe, W., Meisenheimer, K., Röttgering, H. J. A., et al. 2004, Nature, 429, 47
Kuraszkiewicz, J. K., Wilkes, B. J., Hooper, E. J., et al. 2003, ApJ, 590, 128
Kuraszkiewicz, J., Wilkes, B. J., Schmidt, G., et al. 2009, ApJ, 692, 1143
Lampton, M., Margon, B., & Bowyer, S. 1976, ApJ, 208, 177
Lusso, E., Comastri, A., Vignali, C., et al. 2010, A&A, 512, A34
Maiolino, R., Mignoli, M., Pozzetti, L., et al. 2006, A&A, 445, 457
Maiolino, R., Shemmer, O., Imanishi, M., et al. 2007, A&A, 468, 979
Makovoz, D., & Marleau, F. R. 2005, PASP, 117, 1113
Marconi, A., & Hunt, L. K. 2003, ApJ, 589, L21
Marconi, A., Risaliti, G., Gilli, R., et al. 2004, MNRAS, 351, 169
Martínez-Sansigre, A., Rawlings, S., Lacy, M., et al. 2005, Nature, 436, 666

McLure, R. J., & Dunlop, J. S. 2004, MNRAS, 352, 1390
Merloni, A., Bongiorno, A., Bolzonella, M., et al. 2010, ApJ, 708, 137
Mignoli, M., Pozzetti, L., Comastri, A., et al. 2004, A&A, 418, 827
Nenkova, M., Ivezić, Ž., & Elitzur, M. 2002, ApJ, 570, L9
Nenkova, M., Sirocky, M. M., Ivezić, Ž., & Elitzur, M. 2008, ApJ, 685, 147
Perola, G. C., Puccetti, S., Fiore, F., et al. 2004, A&A, 421, 491
Peterson, B. M., Ferrarese, L., Gilbert, K. M., et al. 2004, ApJ, 613, 682
Pier, E. A., & Krolik, J. H. 1992, ApJ, 401, 99
Pier, E. A., & Krolik, J. H. 1993, ApJ, 418, 673
Polletta, M., Weedman, D., Hönig, S., et al. 2008, ApJ, 675, 960
Pozzi, F., Vignali, C., Comastri, A., et al. 2007, A&A, 468, 603
Renzini, A. 2006, ARA&A, 44, 141
Richards, G. T., Lacy, M., Storrie-Lombardi, L. J., et al. 2006, ApJS, 166, 470
Rigby, J. R., Rieke, G. H., Pérez-González, P. G., et al. 2005, ApJ, 627, 134
Risaliti, G., Elvis, M., & Nicastro, F. 2002, ApJ, 571, 234
Rodighiero, G., Gruppioni, C., Civano, F., et al. 2007, MNRAS, 376, 416
Salpeter, E. E. 1955, Vistas in Astronomy, 1, 283
Shen, Y., Greene, J. E., Strauss, M. A., Richards, G. T., & Schneider, D. P. 2008, ApJ, 680, 169
Shields, G. A., Salviander, S., & Bonning, E. W. 2006, New Astron. Rev., 50, 809
Silva, L., Maiolino, R., & Granato, G. L. 2004, MNRAS, 355, 973
Spergel, D. N., Verde, L., Peiris, H. V., et al. 2003, ApJS, 148, 175
Stark, A. A., Gammie, C. F., Wilson, R. W., et al. 1992, ApJS, 79, 77
Steffen, A. T., Strateva, I., Brandt, W. N., et al. 2006, AJ, 131, 2826
Vasudevan, R. V., & Fabian, A. C. 2009, MNRAS, 392, 1124
Vasudevan, R. V., Fabian, A. C., Gandhi, P., Winter, L. M., & Mushotzky, R. F. 2010, MNRAS, 402, 1081
Vignali, C., Brandt, W. N., & Schneider, D. P. 2003, AJ, 125, 433
Vignali, C., Pozzi, F., Fritz, J., et al. 2009, MNRAS, 395, 2189 (V09)
Weedman, D., Polletta, M., Lonsdale, C. J., et al. 2006, ApJ, 653, 101
Witt, H. J., Czerny, B., & Zycki, P. T. 1997, MNRAS, 286, 848
Zamorani, G., Henry, J. P., Maccacaro, T., et al. 1981, ApJ, 245, 357
Zombeck, M. V. 1990, Handbook of space astronomy and astrophysics (Cambridge University Press)